The Astrophysical Journal, 976:204 (16pp), 2024 December 1 https://doi.org/10.3847/1538-4357/ad865b

Spectropolarimetric Inversion in Four Dimensions with Deep Learning (SPIn4D). I. Overview, Magnetohydrodynamic Modeling, and Stokes Profile Synthesis

Kai E. Yang (杨凯)[1], Lucas A. Tarr[2], Matthias Rempel[3], S. Curt Dodds[4], Sarah A. Jaeggli[2], Peter Sadowski[5], Thomas A. Schad[2], Ian Cunnyngham[4], Jiayi Liu (刘嘉奕)[4], Yannik Glaser[5], and Xudong Sun (孙旭东)[1]
[1] Institute for Astronomy, University of Hawai'i at Mānoa, Pukalani, HI 96768, USA; xudongs@hawaii.edu
[2] National Solar Observatory, Pukalani, HI 96768, USA
[3] High Altitude Observatory, NSF National Center for Atmospheric Research, Boulder, CO 80307, USA
[4] Institute for Astronomy, University of Hawai'i at Mānoa, Honolulu, HI 96822, USA
[5] Department of Information and Computer Sciences, University of Hawai'i at Mānoa, Honolulu, HI 96822, USA
Received 2024 July 27; revised 2024 October 2; accepted 2024 October 8; published 2024 November 25

Abstract

The National Science Foundation's Daniel K. Inouye Solar Telescope (DKIST) will provide high-resolution, multiline spectropolarimetric observations that are poised to revolutionize our understanding of the Sun. Given the massive data volume, novel inference techniques are required to unlock its full potential. Here, we provide an overview of our "SPIn4D" project, which aims to develop deep convolutional neural networks (CNNs) for estimating the physical properties of the solar photosphere from DKIST spectropolarimetric observations. We describe the magnetohydrodynamic (MHD) modeling and the Stokes profile synthesis pipeline that produce the simulated output and input data, respectively. These data will be used to train a set of CNNs that can rapidly infer the four-dimensional MHD state vectors by exploiting the spatiotemporally coherent patterns in the Stokes profile time series. Specifically, our radiative MHD model simulates the small-scale dynamo actions that are prevalent in quiet-Sun and plage regions. Six cases with different mean magnetic fields have been explored; each case covers six solar-hours, totaling 109 TB in data volume. The simulation domain covers at least $25 \times 25 \times 8$ Mm, with $16 \times 16 \times 12$ km spatial resolution, extending from the upper convection zone up to the temperature minimum region. The outputs are stored at a 40 s cadence. We forward model the Stokes profile of two sets of Fe I lines at 630 and 1565 nm, which will be simultaneously observed by DKIST and can better constrain the parameter variations along the line of sight. The MHD model output and the synthetic Stokes profiles are publicly available, with 13.7 TB in the initial release.

Unified Astronomy Thesaurus concepts: Magnetic fields (994); Solar photosphere (1518); Spectropolarimetry (1973); Active solar chromosphere (1980); Convolutional neural networks (1938); Magnetohydrodynamical simulations (1966)

1. Introduction

The solar photosphere, a dynamic layer characterized by diverse plasma and magnetic states, plays an essential role in solar astronomy. Within this layer, processes such as magnetic field emergence, convection, and energy and helicity injection are continuously ongoing and define the structure and evolution of the outer solar atmosphere and the rest of the heliosphere. Understanding the photospheric plasma is therefore key to understanding solar activity. The photosphere is dynamically described by the magnetohydrodynamic (MHD; E. Priest 2014) equations, which govern the four-dimensional (4D; three for space plus one for time) evolution of the MHD state vector: the magnetic $\boldsymbol{B}$ and velocity $\boldsymbol{v}$ vector fields and the scalar density ρ and pressure p (or temperature T) fields. In addition to the MHD equations, radiative transfer plays a dual role in the system. On the one hand, it directly modifies the thermodynamic evolution of the plasma relative to basic MHD via the emission and absorption of photons, while on the other hand, the resulting spectrum that reaches the far field (e.g., at ground- and space-based telescopes) encodes the state of the system and thus provides crucial diagnostics of the photospheric plasma (I. Hubeny & D. Mihalas 2015). Notably, the Zeeman and Hanle effects encode the state of the magnetic field in polarized radiation, provided it can be properly interpreted (J. Stenflo 1994; J. C. del Toro Iniesta 2007).

The Daniel K. Inouye Solar Telescope (DKIST; T. R. Rimmele et al. 2020), established by the National Science Foundation, opened a new era in solar observation with the commencement of its scientific operations in 2022. Boasting the world's largest aperture for solar studies (4 m), DKIST enables unprecedentedly sharp observations (down to 0.″03 or 25 km), with the excellent seeing conditions on Haleakalā and its advanced adaptive optics system. Both the design of the telescope and its instrumentation suite enable measurements of polarized signals with unparalleled accuracy (approximately 5×10^{-4}; T. R. Rimmele et al. 2020; A. G. de Wijn et al. 2022; S. A. Jaeggli et al. 2022; D. M. Harrington et al. 2023). Its large aperture means it can match the signal-to-noise ratio (SNR) of deep-exposure quiet-Sun observations by the Hinode/Spectro-Polarimeter (SP; B. W. Lites et al. 2008) in a fraction of the time (∼60 s versus ∼1 s). Equipped with cutting-edge instruments like the Visible Spectro-Polarimeter (ViSP; A. G. de Wijn et al. 2022), the Diffraction-Limited Near-Infrared Spectro-Polarimeter (DL-NIRSP; S. A. Jaeggli et al. 2022), the Cryogenic Near-Infrared Spectropolarimeter (T. A. Schad et al. 2023), and the Visible Tunable Filter (W. Schmidt et al. 2016), DKIST has the capability of exploring various solar regions, from the

photosphere and chromosphere to the corona. Here, we focus on the capabilities of the DL-NIRSP, which currently observes in the near-infrared spectrum using integrating fiber-optic integral field units (IFUs) that enable the simultaneous collection of multiline Stokes profiles across a continuous field of view (FOV).[6] This feature significantly enhances our ability to measure and analyze solar phenomena in detail, particularly the magnetic properties of the small-scale structures.

With the help of the above new facilities, spectropolarimetric observations (typically in the form of wavelength-dependent Stokes profiles) for solar physics will significantly expand in the near future. These advanced observations are sensitive to the plasma state variables across the solar atmosphere (J. C. del Toro Iniesta & B. Ruiz Cobo 2016; L. Bellot Rubio & D. Orozco Suárez 2019 and references therein), offering a unique tool for probing the solar environment at different heights through sophisticated inversion techniques, whereby the multidimensional state of the plasma is inferred from 2D maps of the polarized spectra (B. Ruiz Cobo & J. C. del Toro Iniesta 1992; A. Asensio Ramos et al. 2008; H. Socas-Navarro et al. 2015; I. Milić & M. van Noort 2018; A. Asensio Ramos & C. J. Diaz Baso 2019; J. M. Borrero et al. 2019; J. de la Cruz Rodriguez et al. 2019; A. Pastor Yabar et al. 2019; C. Quintero Noda et al. 2021, 2023; B. Ruiz Cobo et al. 2022). For example, initial DKIST/ViSP data measurements of magnetic fields in both quiet and plage regions highlight the utility of spectropolarimetric observation in probing plasma dynamics in otherwise inaccessible environments (J. M. da Silva Santos et al. 2023; R. J. Campbell et al. 2023; D. Kuridze et al. 2024). Developing good inversion techniques is thus required to tackle a host of unanswered questions in both solar and plasma physics in general; for instance, probing the mechanisms behind local magnetic dynamos (A. Vögler & M. Schüssler 2007; J. O. Stenflo 2012; J. W. Lord et al. 2014; M. Rempel 2014), understanding the flux of helicity and energy across the solar surface (Y. Liu & P. W. Schuck 2012; Y. Liu et al. 2014, 2023; B. T. Welsch 2015; E. Lumme et al. 2019; P. W. Schuck & S. K. Antiochos 2019; J. K. Thalmann et al. 2021), and unraveling the magnetic foundations necessary for solar eruptions and coronal heating (S. K. Antiochos 1998; S. K. Antiochos et al. 1999; R. L. Moore et al. 2001; E. R. Priest & T. G. Forbes 2002; X. Sun et al. 2013; H. Wang et al. 2015, 2017; C. Liu et al. 2016; L. P. Chitta et al. 2017; P. F. Wyper et al. 2017; T. Samanta et al. 2019).

Despite recent advancements in inversion technology, creating accurate 3D reconstructions of the solar atmosphere still remains a challenge. In particular, knowledge of the physical variables' distribution on a spatial grid is crucial for the calculation of differential quantities that define the key parameters of the system, e.g., the electric current, Lorentz force, helicity, energy flux, and so on. Most current inversion techniques return the physical state of the plasma on an optical depth τ grid rather than on a spatial grid. Converting to a physical grid along the line of sight (LOS) involves the additional steps of resolving the ambiguity in the inverted magnetic azimuth angle, reconstructing the atmosphere based on dynamic/static assumptions, and defining a vertical offset between each (assumed) independent LOS (A. Pastor Yabar et al. 2019; J. M. Borrero et al. 2019, 2021; J. M. Borrero & A. Pastor Yabar 2023). The spatiotemporal information of the time-series observations is governed by the MHD equations. Once incorporated, they can help resolve the LOS spatial grid and ambiguity issues while also enhancing the physical accuracy of inversions. However, integrating this information is challenging in traditional 1D inversion techniques based on sophisticated radiative transfer methods. These challenges are exacerbated by the need for powerful computers to process the data and the complex work of creating accurate solar models that match up with scientific laws over time, e.g., Newton's laws and Maxwell's equations. Moreover, the arrival of powerful telescopes like DKIST, which can generate about 20 TB of data every day, makes these challenges even greater, testing the limits of our current technology. This huge amount of data highlights the urgent need for innovative and efficient methods to handle and analyze large volumes of solar Stokes profile data in the DKIST era.

On the other hand, deep learning (DL), a specialized branch of machine learning (ML), has shown exceptional efficacy in deriving approximate inferences from physics models (P. Sadowski & P. Baldi 2018; J. Brehmer et al. 2020). The rapid progress of ML in solar physics, especially through DL's application to Stokes inversion, would significantly enhance our understanding and analytical abilities (A. Asensio Ramos et al. 2023 and references therein). Recent studies have highlighted the effectiveness of convolutional neural networks (CNNs; A. Asensio Ramos & C. J. Diaz Baso 2019; I. Milić & R. Gafeira 2020; R. Gafeira et al. 2021; R. E. L. Higgins et al. 2021, 2022; B. A. Chappell & T. M. D. Pereira 2022; R. Centeno et al. 2022; S. Rahman et al. 2023, 2024; L. Mistryukova et al. 2023) and other advanced ML algorithms (M. G. Bobra & S. Couvidat 2015; M. G. Bobra & S. Ilonidis 2016; K. Florios et al. 2018; X. Huang et al. 2018; N. Nishizuka et al. 2018; A. Sainz Dalda et al. 2019; C. J. Díaz Baso et al. 2022; A. Vicente Arévalo et al. 2022; R. Jarolim et al. 2023, 2024a, 2024b; G. T. Goodwin et al. 2024) in processing a wide array of solar observations, ranging from the quiet Sun to dynamic solar flares and coronal mass ejections. These models have shown promising results in enhancing accuracy and efficiency, notably outpacing traditional methods in speed without sacrificing analytical complexity. Furthermore, the DL methods can enhance spatial resolution and image denoising, improving the capability of observing small structures (A. Asensio Ramos et al. 2018; C. J. Díaz Baso & A. Asensio Ramos 2018; C. J. Díaz Baso et al. 2019; S. Rahman et al. 2020; W. Song et al. 2022; H. Eklund 2023). With the help of time-series observations, it also effectively resolves solar surface flows, with the DeepVel code (A. Asensio Ramos et al. 2017) demonstrating superior performance compared to conventional methods in analyzing these small-scale structures (B. Tremblay et al. 2018).

Most of the aforementioned ML models are supervised learning models, requiring a large volume of training data to derive a relationship between the input and target data. Fortunately, modern numerical MHD simulations can now accurately mimic various solar phenomena (M. C. M. Cheung et al. 2010, 2019; M. Rempel 2012, 2014; F. Chen et al. 2017, 2023a, 2023b) and therefore allow the generation of extensive and realistic data sets for DL training. Once trained, DL inversion models are extremely fast to run. For example, in the pioneering work of A. Asensio Ramos & C. J. Diaz Baso (2019), they train 2D CNN models using a radiation-MHD simulation of a sunspot and synthesized Stokes profiles. When applied to observational data from the Hinode/SP, their CNN model inverts a 512×512 pixel map within $\sim$180 ms, orders

[6] DL-NIRSP recently (winter 2023) swapped the fiber-optic IFU for a newly developed image-slicer. The resulting data products will be functionally equivalent for our purposes, but have increased fidelity.

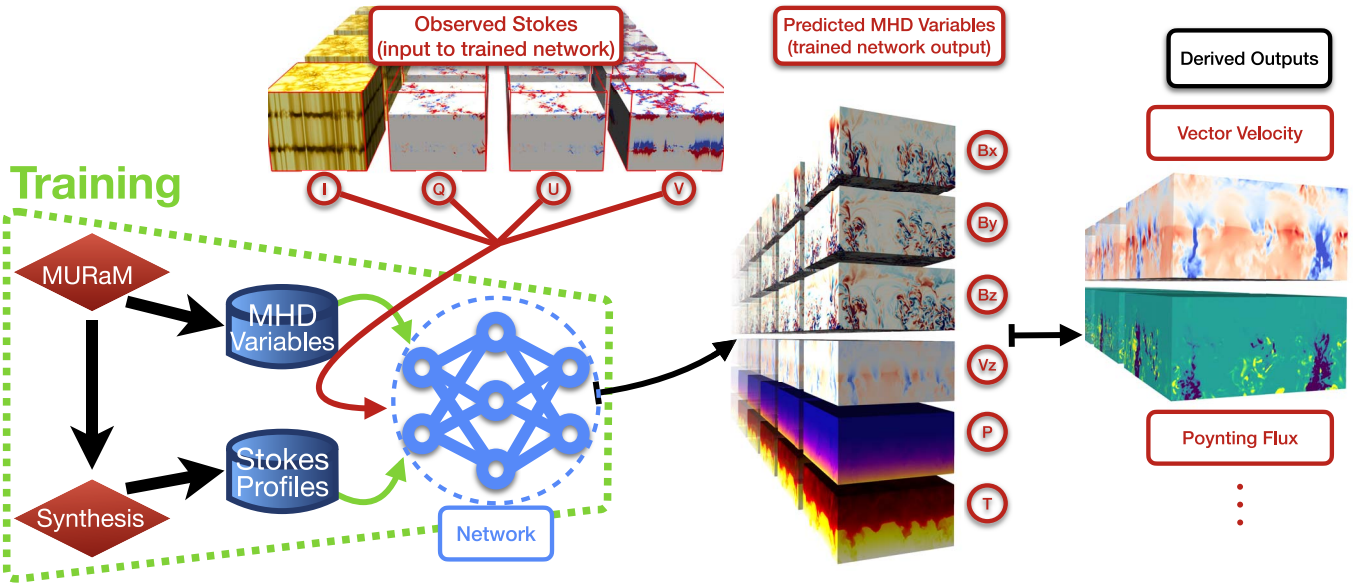

Figure 1. Schematic representation of the SPIn4D model workflow. The core of the model is the DL neural network, highlighted in blue in the middle of the diagram. The network training step is outlined by the broken green line and uses data derived from the MURaM simulations, both the MHD variables themselves and the Stokes profiles (I, Q, U, V) synthesized from the MHD data cubes (green lines). Once trained on the simulated data, observed Stokes data can be input into the network (red arrow) to produce the most likely 3D MHD state as output (labeled "Predicted MHD Variables"). The network may be trained to receive single-time input Stokes data to produce a reduced dimensional output MHD state ($\boldsymbol{B}$, v_z, P, T) or to receive multitime input Stokes data to produce a full-dimensional MHD output, including additional derived outputs, such as vector velocities, Poynting flux, and so on. The network may also be trained to produce the derived outputs directly.

of magnitude faster than current inversion methods. Additionally, the model could recover the 3D MHD variables on a true spatial grid rather than an optical depth grid, and at roughly half the error compared to the Stokes Inversion based on Response functions (SIR; B. Ruiz Cobo & J. C. del Toro Iniesta 1992, 2012) code. It is worth mentioning that A. Asensio Ramos & C. J. Diaz Baso (2019) did not treat the azimuthal ambiguity in the magnetic field directly, but instead solved a reduced problem using a coordinate transformation.

To address the challenges outlined above and take advantage of the potential of DL, we launched the "Spectropolarimetric Inversion in Four Dimensions with Deep Learning" (SPIn4D) project[7] to train CNN models on radiative MHD (RMHD) simulations with a significantly larger data set, i.e., larger domain size, longer evolution, and more cases with a variety of mean magnetic field strengths, compared to previous efforts. As discussed below, this provides more statistically independent snapshots useful for training. Detailed information about the data, including access methods, are publicly available.[8]

Figure 1 presents a schematic overview of the key elements of each phase of the project. Our focus will be on photospheric regions with intermediate field strengths (between quiet Sun and plage or up to a few hundred Gauss when spatially averaged), characterized by relatively simple field geometries. These regions are expected to be prevalent in the initial years of DKIST's operation. Simulations are carried out using the Max-Planck University-of-Chicago Radiative MHD code (MURaM; A. Vögler et al. 2005; M. Rempel et al. 2009; M. C. M. Cheung et al. 2010; M. Rempel 2012, 2014) and take the quiet-Sun small-scale dynamo (SSD) simulation of M. Rempel (2014) as the point of departure. The fact that these MURaM simulations use gray radiative transfer is not expected to impact the results here. As both the training and the evaluation steps use synthetic data, the ML models should simply learn the mapping between the self-consistent inputs and outputs, without regard to the detailed physics. When applying to real observations, however, we do expect ML models trained on more realistic, nongray radiative transfer simulations (A. Vögler 2004) to perform better, at the expense of increased computational costs.

Next, we employ forward modeling of radiative transfer through these simulations, using a new version of the SIR code (SIR3D) and the Departure Coefficient aided Stokes Inversion based on Response Functions (DeSIRe; B. Ruiz Cobo et al. 2022) code to synthesize Stokes profiles for multiline observations. We have selected the well-studied Fe I lines at 630.15, 630.25, 1564.9, and 1565.2 nm due to their significant Landé factors (2.5, 1.67, 3, and 1.53, respectively) and their widespread use in ground- and space-based observations with high Stokes SNR.

The third phase involves developing CNN models that aim to accurately correlate time series of observational data, especially those from the DL-NIRSP instrument at DKIST, with precise 4D MHD states. The models will be rigorously trained and evaluated using the data generated in the first two steps. The ability of this model will be compared with the SIR inversion code as a baseline. Higher-level variables, such as the vector velocity and associated Poynting flux across the photosphere, may be estimated either based on the inversion results, as in conventional methods (e.g., Y. Liu & P. W. Schuck 2012; M. D. Kazachenko et al. 2014), or ultimately directly from our ML models that encode the temporal information with a time series of Stokes profiles as input. In this paper, we focus on the generation of the training data for the SPIn4D project. The paper is organized as follows. Section 2 delves into the specifics of the MURaM SSD

[7] https://ifauh.github.io/SPIN4D/

[8] Several data access methods are offered for Data Release 1 at http://dtn-itc.ifa.hawaii.edu/spin4d/DR1/.

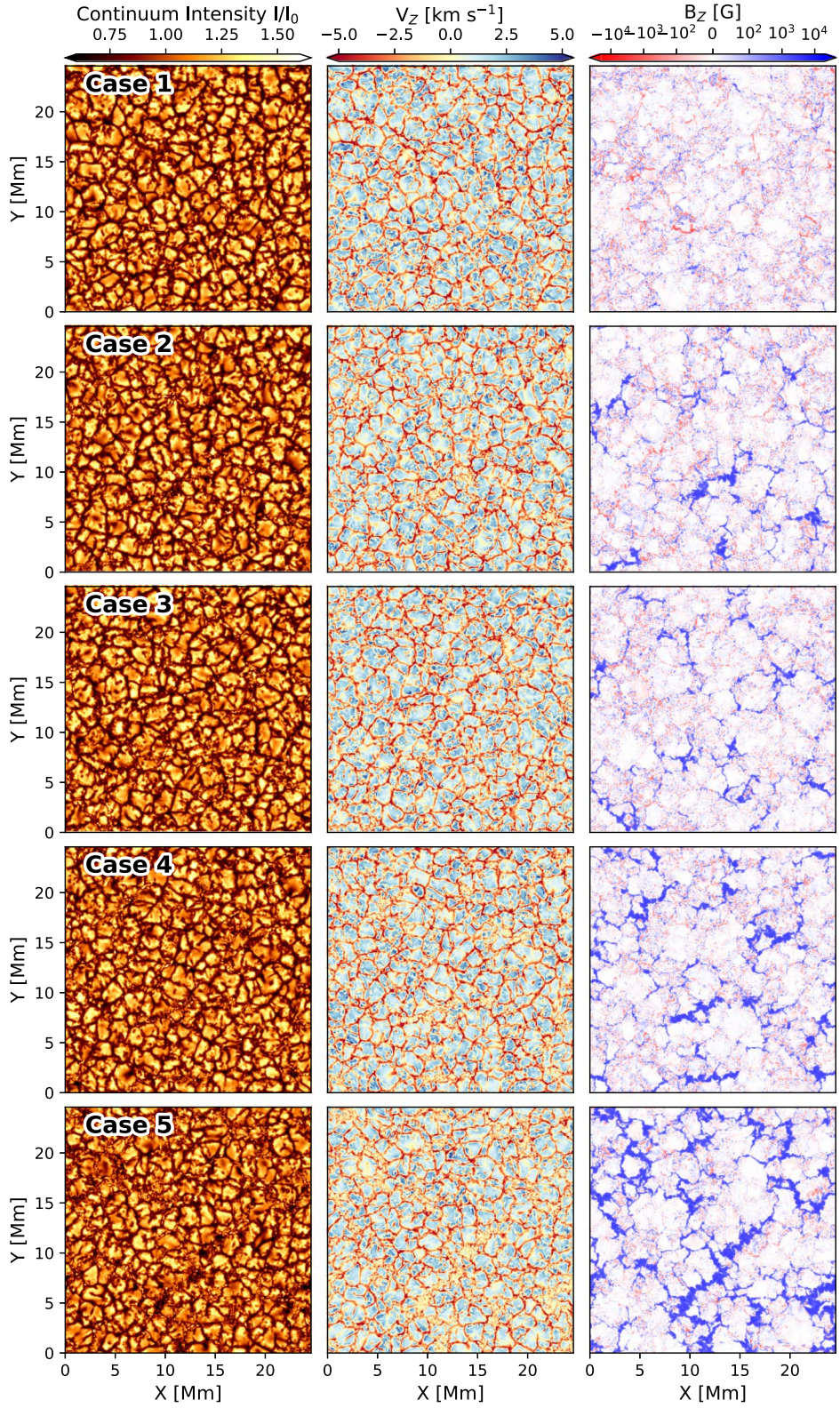

Figure 2. From top to bottom, representative simulation results for Cases 1–5 at simulation times 5.43 hr, 5.59 hr, 5.59 hr, 5.59 hr, and 5.58 hr, respectively. From left to right, the columns show continuum emission at 500 nm, LOS velocity (V_Z), and LOS magnetic induction (B_Z) at an extracted surface of $\log_{10}\tau = 0$, respectively.

simulation. The process of multiline synthesis is explored in Section 3. Section 4 addresses simulation artifacts and their treatment. Finally, a summary is provided in Section 5. Additional details on the pipeline are included in Appendices A and B.

2. Solar Atmosphere Simulation

We ran six RMHD simulations covering a variety of photospheric conditions, ranging from very quiet Sun to fairly strong plage. Synthetic spectropolarimetric observations are

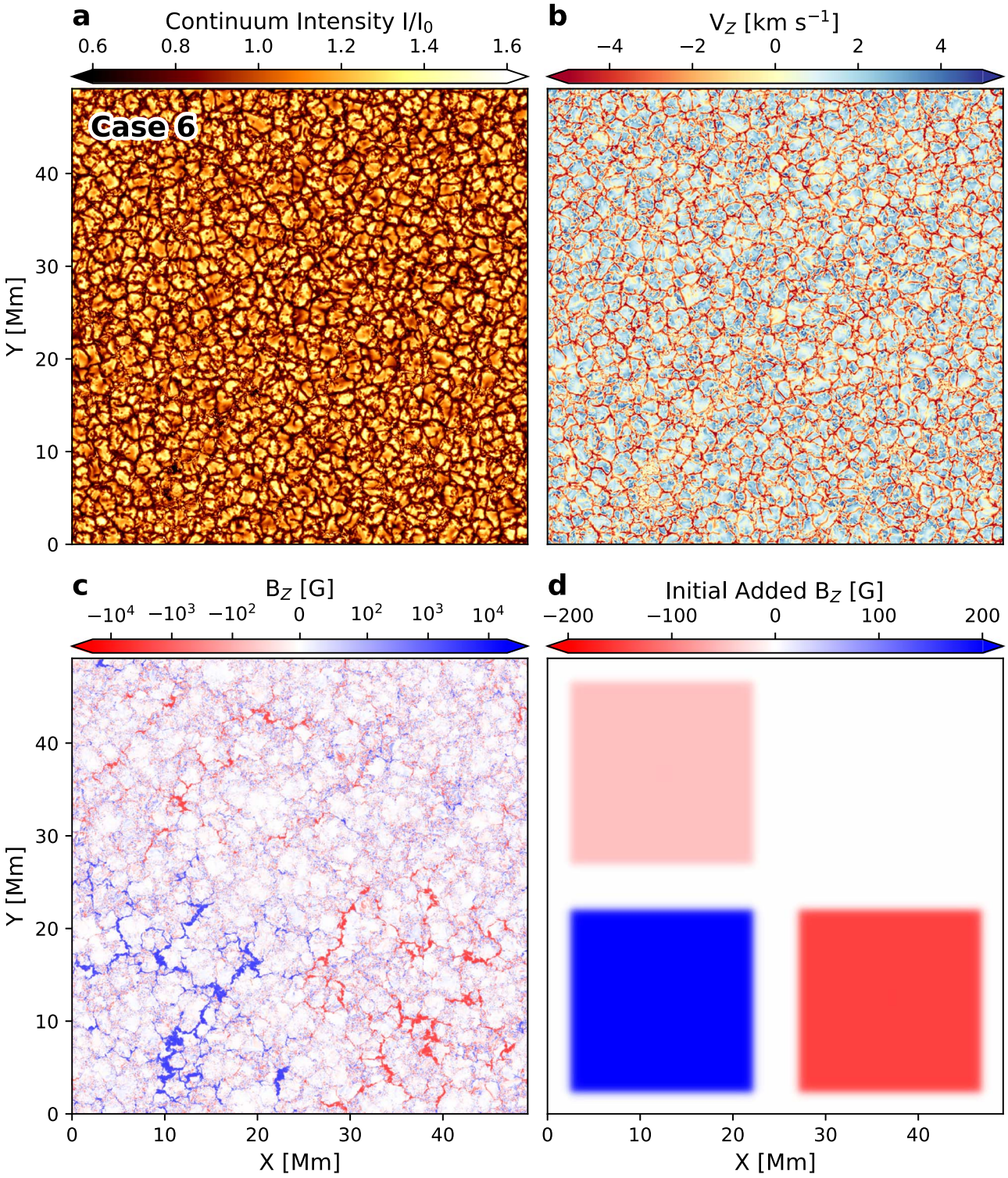

Figure 3. Similar to Figure 2, but for Case 6 at 5.44 hr. Panel (d) shows the additional vertical field added to each quadrant and outlines the mask function.

created by running radiative forward models through the RMHD output (Section 3). The RMHD simulations use the MURaM code (A. Vögler et al. 2005; M. Rempel et al. 2009) and take the relaxed solar atmosphere of the SSD case SSD 016bM from M. Rempel (2014) as their starting point. Compared to M. Rempel (2014), the simulation domain was extended by 500 km in the vertical direction above the photosphere and the vertical grid spacing was reduced from 16 to 12 km. This formed the basis of our Case 1, a straightforward continuation of the SSD O16bM simulation. Cases 2, 4, and 5 simulate regions with increasingly stronger average field strength, introduced as an additional uniform magnetic field to each initial condition's vertical component, B_Z, at strengths of 50 G, 100 G, and 200 G, respectively.

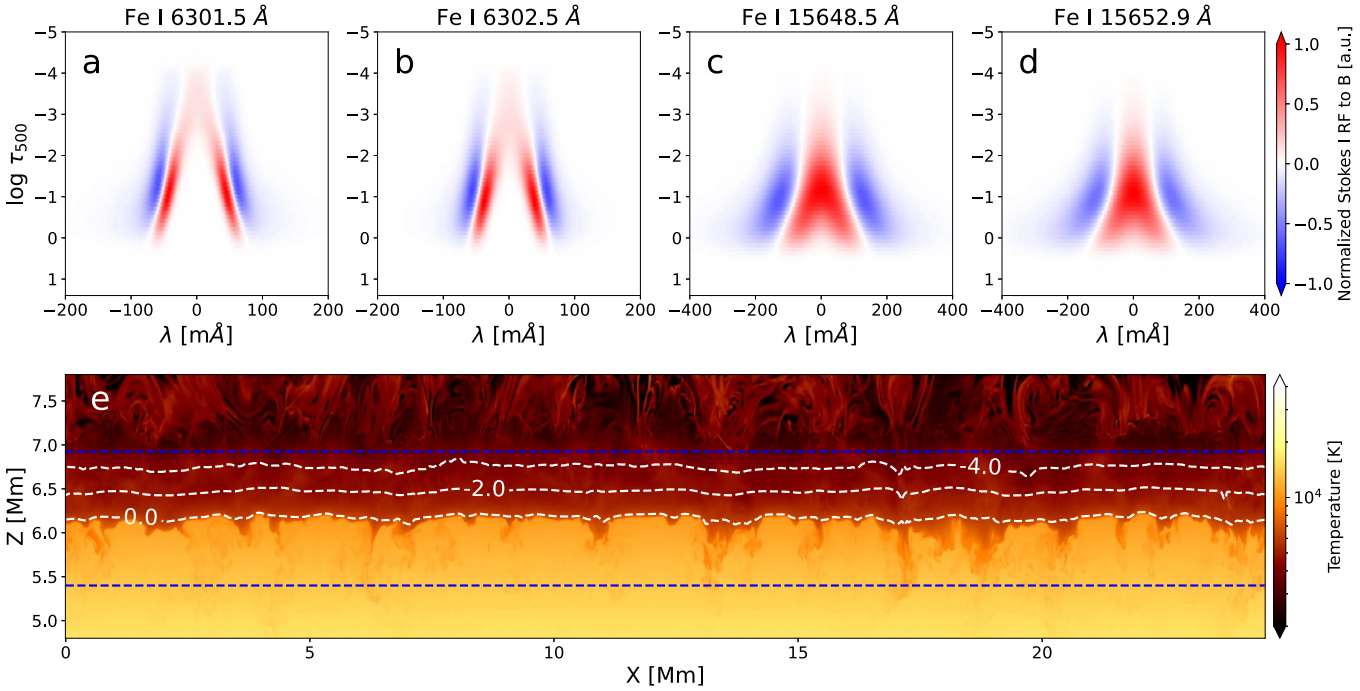

Figure 4. (a)–(d) The response function of Stokes I to the magnetic induction for the four lines used in our study. (e) Temperature distribution on a vertical slice at the middle of the computational domain, $y = 12.28$ Mm, from Case 1 at $t = 5.43$ hr. The three white dashed lines indicate the contours of the logarithm optical depth, $\log_{10}\tau$, with the values of 0, −2, and −4. The two blue dashed lines indicate the subdomain we extracted for the training data set.

Table 1
MHD Simulation Summary

	Modified Field [a] (G)	Duration [b] (hr)	Size [c] (TB)
Case 1	0	5.97	12
Case 2	B_Z: 50	6.21	12
Case 3	$B_{X,Y,Z}$: 50[d]	6.23	12
Case 4	B_Z: 100	6.02	12
Case 5	B_Z: 200	6.04	12
Case 6	B_Z: 200, − 150, − 50[e]	6.20	49

Notes.
[a] The magnetic field added to the relaxed SSD O16bM atmosphere as the initial condition for our simulations.
[b] The physical time of the total simulations for each case.
[c] The total size of the output 3D atmosphere files.
[d] Case 3 has $B_X = B_Y = B_Z = +50$ G.
[e] Case 6 has +200 G, −150 G, and −50 G added to B_Z in three quadrants (see Figure 3).

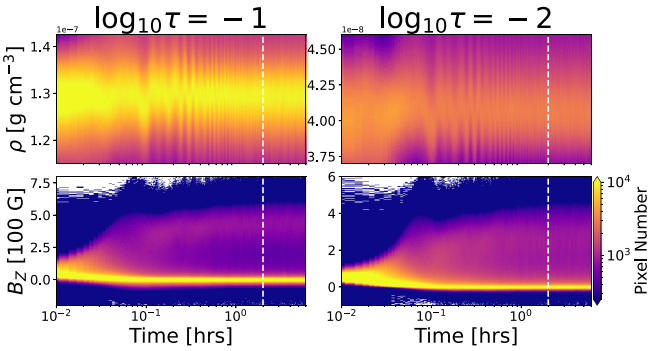

Figure 5. The time-series histogram of the density, ρ, and LOS magnetic field, B_Z, on two surfaces, $\log_{10}\tau = -1$ and −2, calculated for Case 5. The vertical dashed lines indicate the time of 2 hr, after which the simulation has essentially steady-state dynamics.

Case 3 was augmented with an inclined initial magnetic field instead, uniformly set at 50 G across all magnetic components.

The computational domain for Cases 1–5 spanned 24.6 × 24.6 × 8 Mm, with a spatial resolution of 16 × 16 × 12 km. The horizontal grid size is approximately half of the diffraction limit of DKIST. We saved the data output every 40 s to match the expected cadence from the DL-NIRSP observations. The side boundaries of the domain are periodic, the bottom boundary is open for convective flows, as detailed in M. Rempel (2014), and the top boundary applies a potential magnetic field extrapolation in the ghost layers, along with a semi-transparent boundary condition for hydrodynamic variables, i.e., density, velocity, and internal energy. This condition is designed to be open for outflows and closed for inflows, featuring (anti)symmetric settings in the ghost layers for inflows and outflows, respectively. Radiative transfer calculations may be carried out in arbitrary directions through the simulated domain, but for the tasks described in this work, we take the LOS direction to be the simulation Z-direction and use these two interchangeably.

In Figure 2, we show representative simulation output toward the end of each run for Cases 1–5: the 500 nm continuum intensity (left), LOS velocity (V_Z; center), and LOS magnetic field (B_Z; right), each extracted from the layer of optical depth $\log_{10}\tau = 0$ at roughly 5.5 hr into each run, where τ is the optical depth at 500 nm. The increasing initial average field strength in each case forms more and stronger field concentrations, as seen in the right column. The greatest

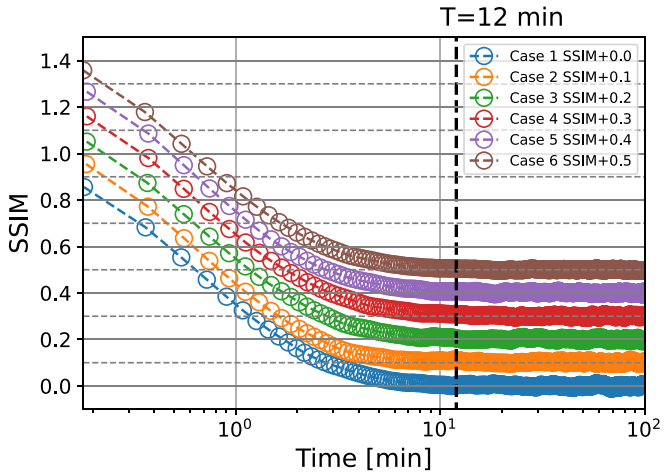

Figure 6. The SSIM of continuum images for different time lag, for all six cases. Each curve is offset vertically by 0.1 for clarity. The vertical dashed line marks our selected cadence of 12 minutes for producing forward-modeled spectral synthesis of independent observations.

addition in Case 5 shows the development of several pores with substantially reduced intensity (left column) associated with the strongest field concentrations (right column), consistent with regions of strong plage on the Sun.

Cases 2–5 each have a net magnetic flux that would mimic coronal hole environments on the actual Sun, with no strong polarities with opposing signs. To account for real-Sun conditions with mixed polarities, we ran an additional Case 6 in a larger domain, created by stitching together four of our modified SSD O16bM initial conditions in the two periodic horizontal directions and then adding additional field of strengths 200 G, −150 G, and −50 G to the vertical component in three quadrants; the fourth quadrant was left in the initial SSD configuration. To avoid discontinuous field strengths, the vertical field added to each quadrant was first multiplied by a mask function that decreases smoothly to zero at each quadrant boundary,

$$\mathrm{mask}(x,\,y) = \frac{1}{4}\left(\tanh\left[\frac{x-0.1}{0.02}\right] - \tanh\left[\frac{x-0.9}{0.02}\right]\right) \times \left(\tanh\left[\frac{y-0.1}{0.02}\right] - \tanh\left[\frac{y-0.9}{0.02}\right]\right), \quad (1)$$

where x and y are normalized coordinates in each field region, before being stitched into the larger domain.

Representative results for Case 6 are shown in Figure 3 around 5.5 hr into the simulation. Figure 3(d) shows the additional vertical field added to each quadrant in the initial condition. After a few solar hours of relaxation, this simulation showed a mix of strong polarities, with the interaction of opposite-polarity patches at the quadrant boundaries (see Figure 3(c)). Portions of this simulation may therefore represent the boundaries of long–decayed active regions.

Each simulation extends over 8 Mm vertically for all cases, from a shallow convection zone to the upper photosphere, represented by 672 grid points. The photospheric Fe I lines that we are interested in form in a relatively narrow layer (∼1 Mm) entirely contained within the simulation domain. In Figures 4(a)–(d), we show the response functions of Stokes I to the magnetic field magnitudes of these lines calculated using SIR. Based on this, and to optimize storage, we selected a range of 128 layers from the simulation interiors for output (at 40 s cadence), specifically from the z grid points 450–577 in the vertical direction, spanning an optical depth range from 10^5 to 10^{-5} and demarcated by the blue dashed lines in Figure 4(e). Comparison with the response functions shows that the extracted region adequately encompasses the formation layers of the Fe I lines of interest. Further details are provided in Section 3.

All Cases 1–6 were simulated for about six physical hours (including the initial two hours of relaxation) and generated a total of 109 TB of output for the 3D MHD variables, including the high-cadence output just described plus occasional snapshots of the full numerical domain. The initial magnetic configuration, total duration, and total output for all cases are summarized in Table 1.

2.1. Initial Relaxation, Convective Turnover Time, and Statistically Independent Training Data

The additions of the vertical fields to the initial conditions of Cases 2–6 represent substantial injections of magnetic energy, and the resulting simulated atmospheres need some time to relax to new steady dynamical states. To illustrate the atmospheric relaxation process, we focus on Case 5, which features the most intense initially added magnetic field at 200 G. Figure 5 presents time-series histograms of physical variables computed at surfaces of $\log_{10}\tau = -1$ and -2 in the left and right columns, respectively, i.e., near the maxima of the response functions of the selected Fe I lines (see Figure 4). The histogram density is displayed as a color scale, with the histogram bin values given on the linear-scaled ordinates and time given on the log-scaled abscissas (to highlight the approach toward a quasi-stationary state). Notably, the density ρ distributions exhibit pronounced oscillations attributable to the initial addition of a uniform B_Z and the resulting imbalance of total pressure. The histograms for B_Z exhibit an initial rapid reduction of pixels with smaller magnitudes (e.g., less than 100 G), as well as a gradual increase of pixels with larger magnitudes (e.g., greater than 250 G). Both distributions stabilize after approximately two hours (vertical dashed line).

With the goal of generating a large training data set suitable for DL, it is important to ensure that each snapshot of training data contains statistically independent information. As the primary spatial feature in our simulations is the solar granulation pattern, we seek to minimize the temporal correlation of this pattern in the final training data set. To achieve this, we assess the lifetime of granules in 500 nm continuum intensity by calculating the structural similarity index measure (SSIM) using the `skimage.metrics.structural_similarity` Python package (Z. Wang et al. 2004). SSIM returns a scalar value for the difference between two images, where a value of 1(0) indicates identical (different) images. For each simulation, we calculate SSIM backward in time, using the final continuum intensity image as a fixed reference image. The results are shown in Figure 6. The curve for each case is offset vertically by 0.1 to aid legibility. Each SSIM curve approaches 0 after about 10 minutes, indicating significant image variation; such is consistent with a granule's lifetime of about 10 minutes. As an

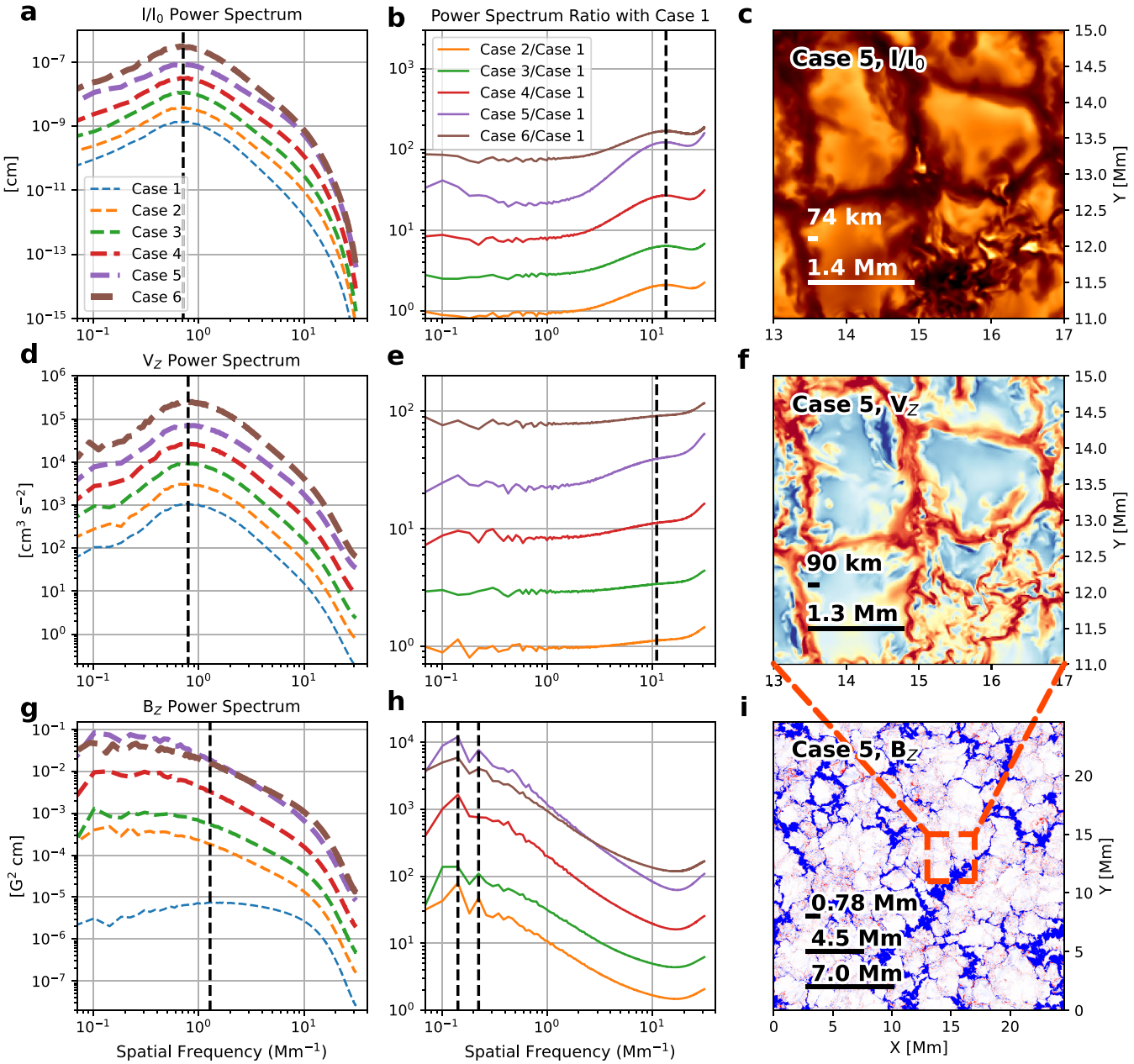

Figure 7. The power spectra of the normalized continuum intensity I/I_0, V_Z, and B_Z at the surface $\log_{10}\tau = 0$, displayed from top to bottom. The left panels (a), (d), and (g) present the direct power spectra for the six cases, each offset vertically by a factor of 3 for better visualization. The vertical dashed lines in panels (a), (d), and (g) mark the local power spectrum peak for Case 1. The middle panels (b), (e), and (h) depict the power spectra ratios of Cases 2–6 to Case 1, with the vertical dashed lines in (b) and (e) indicating the local peak and saddle point for Case 2 at smaller scales, and in (h) the local peak for Case 2 at larger scales. Panels (c), (f), and (i) show lines marking the typical scales of the peak values in their respective spectra overlaid on a representative subregion for each variable. The dashed red box in (i) highlights the FOV seen in panels (c) and (f), to enhance the visualization of the typical spatial scale derived from the power spectrum.

Table 2
Stokes Profile Data

Fe I	6301–6302 Å	15648–15652 Å
Line Range (Å)	6300.8–6303.3	15646.8–15654.8
$\Delta\lambda$ (mÅ)	8.945	31.376
SIR Data Size (TB)	5.5	5.1
DeSIRe Data Size (TB)	5.5	5.1

initial attempt, we selected a 12 minutes cadence to generate the synthesized Fe I lines for our training data set. More discussion on this choice can be found in Section 3.

2.2. On the Range of Simulated Solar Environments

Cases 1–5 represent a range of conditions found on the Sun, differentiated solely by the strength of the uniform magnetic field added to the base SSD simulation for each case's initial condition; Case 6 extends this with a larger FOV and mixed-polarity regions. The varied conditions produce corresponding differences in the spatial structures of the resulting granulation patterns. In Figure 7, we quantify those differences by computing, at the $\log_{10}\tau = 0$ surface, the spatial power spectra of the normalized continuum intensity I/I_0 (first row, panels (a)–(c)), the vertical velocity (second row, panels (d)–(f)), and the vertical magnetic field (third row, panels (g)–(i)). All the curve plots in the log scale in this

Table 3
Atomic Parameters

Wavelength (Å)	Γ_6[a]	Exc. Pot[b] (eV)	log(gf)[c]	Transition Level	α[d]	σ[d] (cm^2)
6301.5012	1.0	3.654	−0.718	5P 2.0–5D 2.0	0.242	2.33543e–14
6302.4936	1.0	3.686	−1.131	5P 1.0–5D 0.0	0.239	2.38024e–14
15648.5088	1.0	5.426	−0.652	7D 1.0–7D 1.0	0.229	2.72747e–14
15652.8809	1.0	6.246	−0.050	7D 5.0–7k 4.0[e]	0.330	4.045e–14

Notes. The atomic parameters are written in SIR format (B. Ruiz Cobo & J. C. del Toro Iniesta 1992).
[a] Enhancement factor to the van der Waals coefficient.
[b] Excitation potential of the lower level.
[c] The logarithm of the multiplicity of the level times the oscillator strength.
[d] The collisional broadening parameters from the quantum mechanical theory of P. S. Barklem et al. (1998).
[e] This transition level is used for the SIR synthesis pipeline, while for DeSIRe, the level is 7D 5.0–(6D4.5)f2k 4.0.

figure are offset vertically by multiplying by a factor of 3 for better visualization. The effect of adding stronger magnetic fields is made clearer by taking the ratio of the power spectra for Cases 2–6 to the SSD case, as shown in the second column (panels (b), (d), and (e)). Together, the power spectra and their ratios reveal that several spatial scales are either present in all cases or notably arise due to the addition of a magnetic field. These scales are indicated in the Fourier domain by vertical dashed lines and in the physical domain by the solid lines drawn on top of a representative subregion for each variable in panels (c), (f), and (i).

Both the continuum intensity and vertical velocity show pronounced peaks at the scale of the granulation pattern, around 1.4 and 1.3 Mm, as seen in panels (a) and (d), respectively. The vertical magnetic field shows a very slight peak for Case 1 only (panel (g)); the peaks are indicated by the vertical dashed line in the first column. From the power spectral ratios presented in the second column, there is a clear trend toward higher power at higher spatial frequencies relative to the SSD case and a generally steeper slope for cases with a greater added magnetic field strength. In the continuum intensity, this trend produces the large peak in ratio at a scale of 74 km, which corresponds to the readily apparent small-scale intergranular bright points seen in Figure 7(c). There is no peak in ratio in the power spectra of V_Z, but instead a saddle point at a scale of 90 km Figure (7(e)), which is the width of the intergranular lanes.

Turning our attention to the power spectrum of B_Z, the only apparent peak occurs for Case 1 and has a size of 0.78 Mm, i.e., roughly half of the granule size as measured in either continuum intensity or velocity. Surprisingly, as more flux is added to the simulation, the magnetic field becomes more ordered (more distinct local peaks) on larger scales. This somewhat mimics a mesogranular morphology and has two local peaks at 4.5 and 7.0 Mm (Figures 7(h) and (i)). However, this might be influenced by interaction with the bottom boundary, since we do not have a deep enough convection layer for the formation of the supergranulation convection pattern (J. W. Lord et al. 2014; J. W. Lord 2014).

3. Stokes Profile Synthesis

We calculated synthetic Stokes data for each case at the statistically independent 12 minutes cadence after the initial 2 hr relaxation period, as determined in Section 2. For the Stokes profiles data set, we selected two Fe I line pairs in the 630 and 1565 nm range, originating from the deep and upper layers of the photosphere, respectively. These lines, whose response functions are depicted in Figures 4(a)–(d), are pivotal in diagnosing the photospheric magnetic field (see L. Bellot Rubio & D. Orozco Suárez 2019 and references therein). Employing a multiline diagnostic approach with these lines will facilitate a comprehensive understanding of the 3D photospheric structure.

The output wavelength sampling for the synthesis was chosen to match the capabilities of the DL-NIRSP instrument, as detailed in S. A. Jaeggli et al. (2022). For the 630 nm spectral window, the DL-NIRSP has a nominal bandpass (derived from the combination of a narrowband filter and spectral mask) of 6.4 Å, a spectral sampling rate of approximately 17.9 mÅ per pixel, and a point-spread function (PSF) with an FWHM of about 40 mÅ. Our synthesis was performed at half the DL-NIRSP sample step, about 8.945 mÅ, covering a range from 6300.8521 Å to 6303.3119 Å across 275 steps. These settings fully cover both lines and extend well into the continuum on either side.

Similarly, for the 1565 nm Fe I line pair, the DL-NIRSP has a nominal bandpass of 16.1 Å, a spectral sampling rate of 62.9 mÅ per pixel, and a PSF with FWHM of 125.8 mÅ. We again synthesized at double the DL-NIRSP spectral sampling, 31.376 mÅ, covering a wavelength range of 15646.875–15654.876 Å with 255 steps. The settings for both line pairs are detailed in Table 2.

We performed the spectral synthesis using two different codes. First, for forward synthesis under local thermal equilibrium (LTE) conditions, we used the 3D version of SIR (B. Ruiz Cobo & J. C. del Toro Iniesta 1992; A. Asensio Ramos & C. J. Diaz Baso 2019). To align with our data set and coordinate system, the code underwent several adaptations, with the revised version accessible on GitHub[9] and details of the modifications described in Appendix A. Acknowledging the significance of non-LTE effects, as identified in the research by H. N. Smitha et al. (2020, 2021), we also integrated the DeSIRe code (B. Ruiz Cobo et al. 2022), along with the parallel Python wrapper outlined by R. Gafeira et al. (2021), into our software pipeline. This approach facilitated the generation of non-LTE Stokes profiles for our chosen lines. The elemental abundance data for an SIR source is from N. Grevesse & A. J. Sauval (1998), which is consistent with that used in the MURaM simulation. For DeSIRe, we use the updated abundance data from M. Asplund et al. (2009). The atomic parameters for the Fe I lines are detailed in Table 3. The resulting synthesized spectral data sets are illustrated in Figure 8.

Cases 2–5 are characterized by a dominant positive magnetic flux. To account for the equally possible input of negative polarity,

[9] https://github.com/ifauh/par-sir

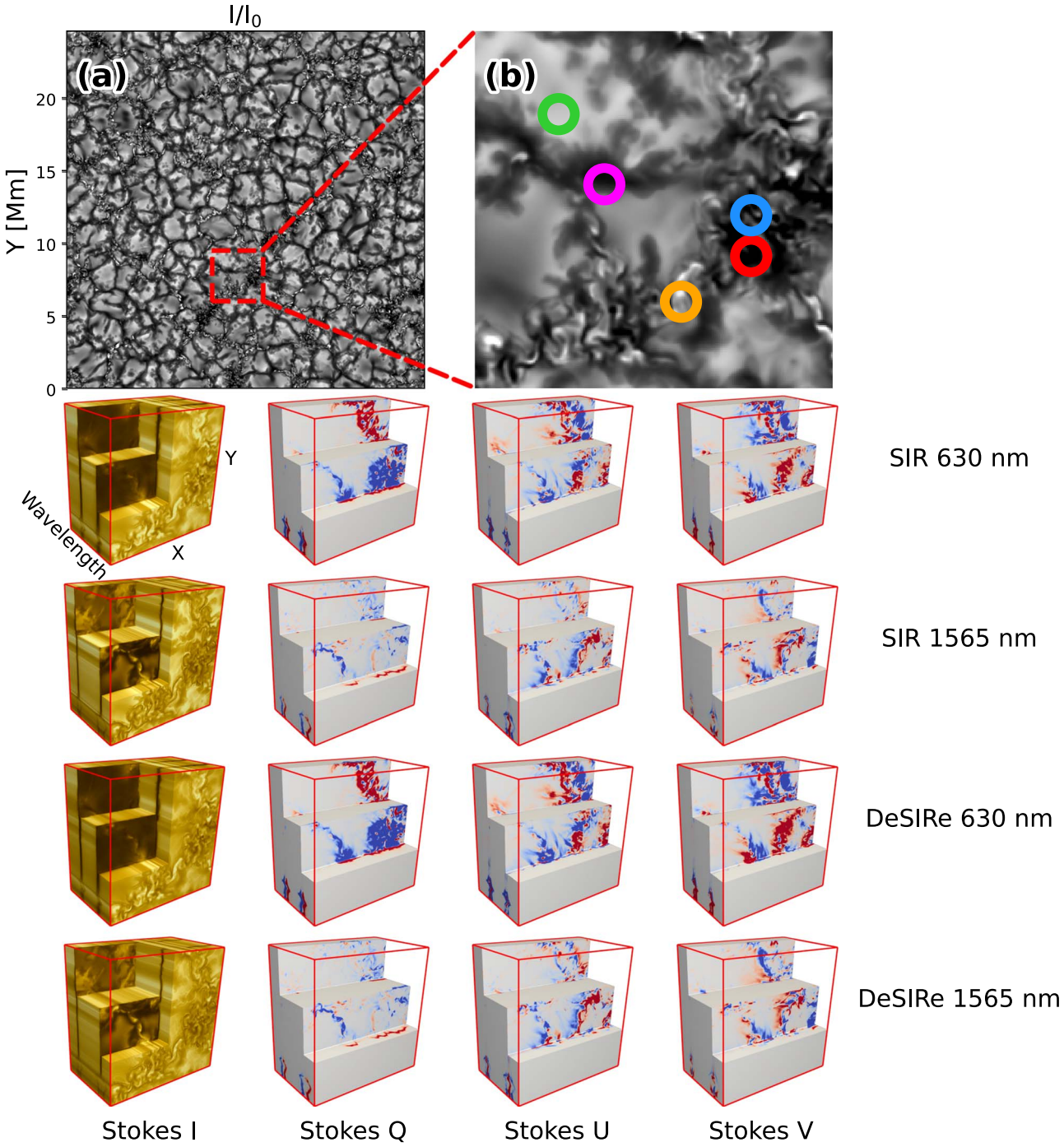

Figure 8. Example synthesized spectropolarimetric data computed for a single snapshot of the Case 5 MHD simulation at $t = 5.6$ hr; the 3D data cubes show a subset of the output for both spectral line pairs and both forward-modeling codes. The red box in panel (a) marks the FOV of the 3D data cubes. Panel (b) shows the zoom-in view of the subset, with the colorized circles indicating locations representative of typical Stokes profiles, as presented in Figure 9.

we manually flip the signs of the magnetic field and calculate a second set of synthetic profiles for each data set. Note that the plasma evolution under the ideal MHD equations remains unchanged when the signs of all three magnetic field components are inverted. This approach allows for random selection between the original and flipped magnetic fields during training of the ML model, effectively minimizing the possible bias from the magnetic field polarity in the resulting neural network model. In total, we generated a collection of 20 TB of Stokes profiles for both SIR and DeSIRe, with and without magnetic field flipping, covering 210 dynamically independent snapshots.

Stokes profiles for five representative locations are shown in Figure 9, corresponding to Case 5 at $t = 5.6$ hr. The first row (panels (b)–(e)) and second row (panels (f)–(i)) present the Stokes profiles for the Fe I 630 and 1565 nm line pairs from the SIR code. The third row (panels (j)–(m)) and fourth row (panels (m)–(q)) present the differences between the synthesized profiles from SIR and DeSIRe, demonstrating minimal discrepancies (note the scale difference between the upper and lower rows). Figure 10 presents the joint distribution between the SIR and DeSIRe synthesized Stokes profiles for the 630 nm line pair for the same data set, with the SIR results shown on the abscissa and DeSIRe on the ordinate

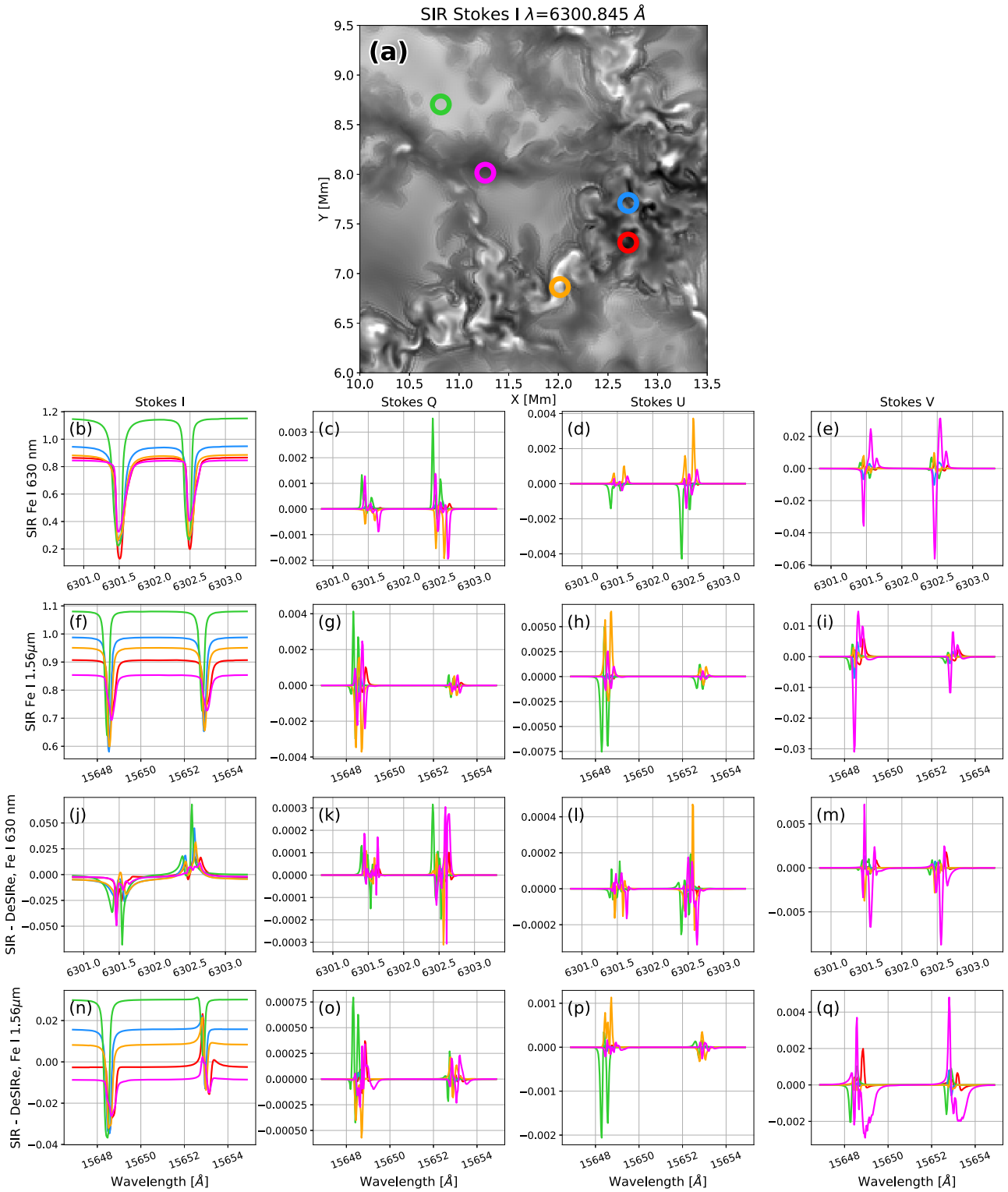

Figure 9. Illustration of the synthesized Stokes profiles from SIR. (a) Intensity of SIR Stokes I at continuum wavelength, with locations of representative Stokes profiles marked by colored circles. Panels (b)–(e) and (f)–(i) show the Stokes profiles for the 630 nm and 1565 nm lines, respectively. Panels (j)–(m) and (n)–(q) detail the differences between the SIR and DeSIRe synthesized profiles, i.e., $I_{\rm SIR} - I_{\rm DeSIRe}$.

for each panel. The red dashed curve marks the one-to-one line. From top to bottom, the rows compare wavelengths in the blue wing, line core, and red wing of the 630.15 nm line, followed by similar plots for the 630.25 nm line. The Pearson correlation of the Stokes I and V is always greater than 0.99, while the linear polarizations (Q and U) show a slightly smaller correlation, $R \approx 0.96$. Figure 13 shows the analogous comparison for the 1565 nm line pair, in Appendix A. The high correlation suggests that the results from the two synthesis codes are in qualitative agreement. The differences can be owing in part to the LTE versus non-LTE treatment of line formation or the different opacity packages.

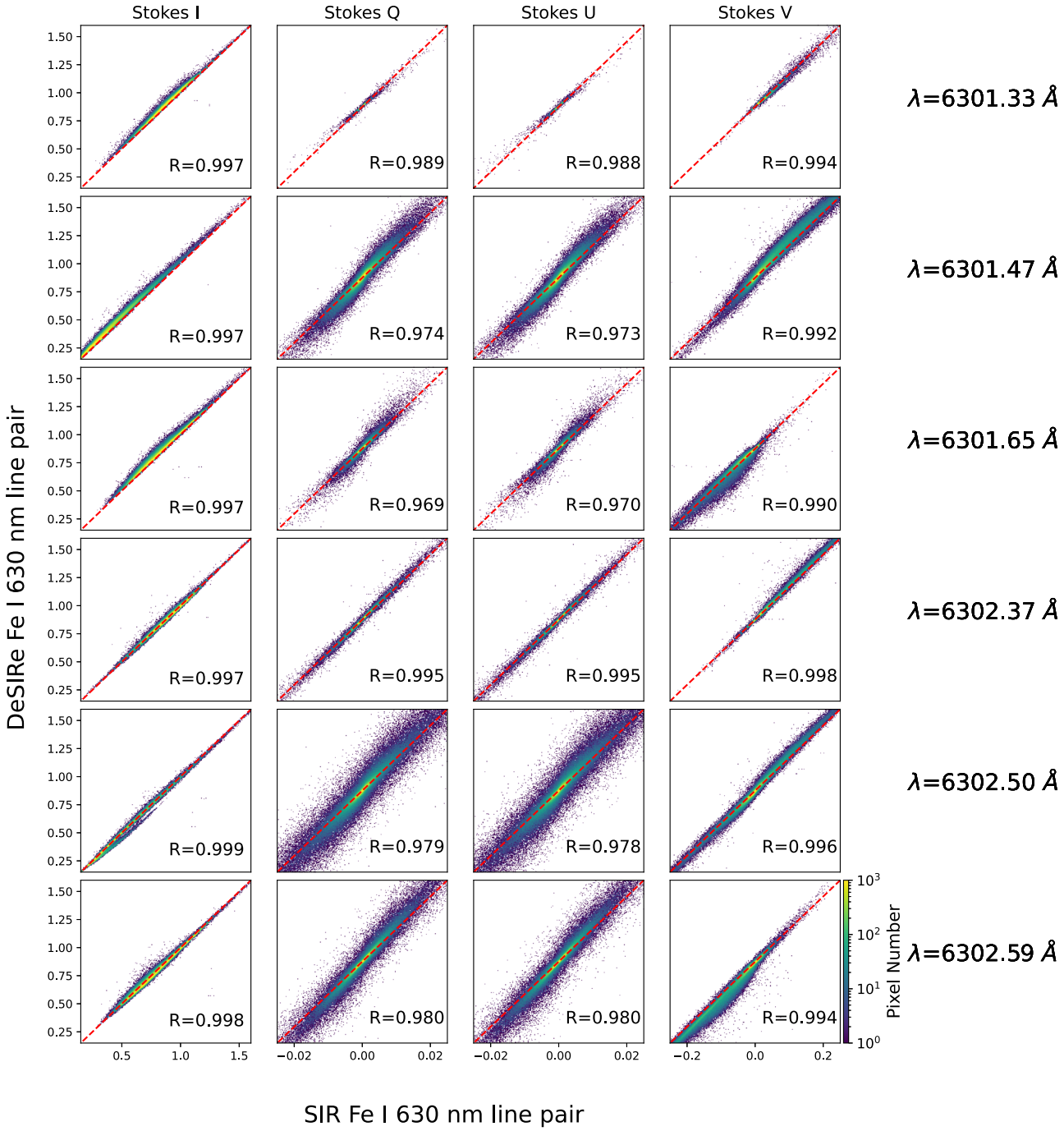

Figure 10. Comparison of the Stokes data from SIR and DeSIRe for the 630 nm line from Case 5 with $t = 5.6$ hr, focusing on the wings and cores. The colors represent the pixel count in the 2D histogram. The dashed red lines denote the line of identity, indicating perfect agreement between the two sets of data. The corresponding Pearson correlation coefficients are marked on each panel.

Our analysis revealed discrepancies in the continuum opacity as a function of T and gas pressure $P_{\rm gas}$ between the SIR and MURaM results. Figure 11 contrasts their κ_{500} values. MURaM's values are derived from its own lookup tables (F. Castelli & R. L. Kurucz 2004), while SIR's are calculated with its `PemufromPgT_i` module using T and $P_{\rm gas}$. Both use the same element abundance (N. Grevesse & A. J. Sauval 1998). Notably, in certain optical depth layers where the line is formed (outlined by the colored contours in Figure 11(c)), the opacity from MURaM is slightly larger than that from SIR.

A direction comparison between the MURaM and DeSIRe opacities proves to be difficult. The latter use a different opacity package, from the RH code (H. Uitenbroek 2001). It is calculated under non-LTE conditions, which do not solely depend on local thermal variables. This is expected to cause some difference in the synthetic profiles shown in Figures 9, 10, and 13. As it is out of the scope of the SPIn4D project, we defer a comprehensive investigation of their differences to future work.

4. Artifacts in MHD Simulation and Solutions

Several features of the MHD simulations may require attention when using the simulation database. In all six cases, significant oscillations occur in the upper regions of the simulated atmosphere,

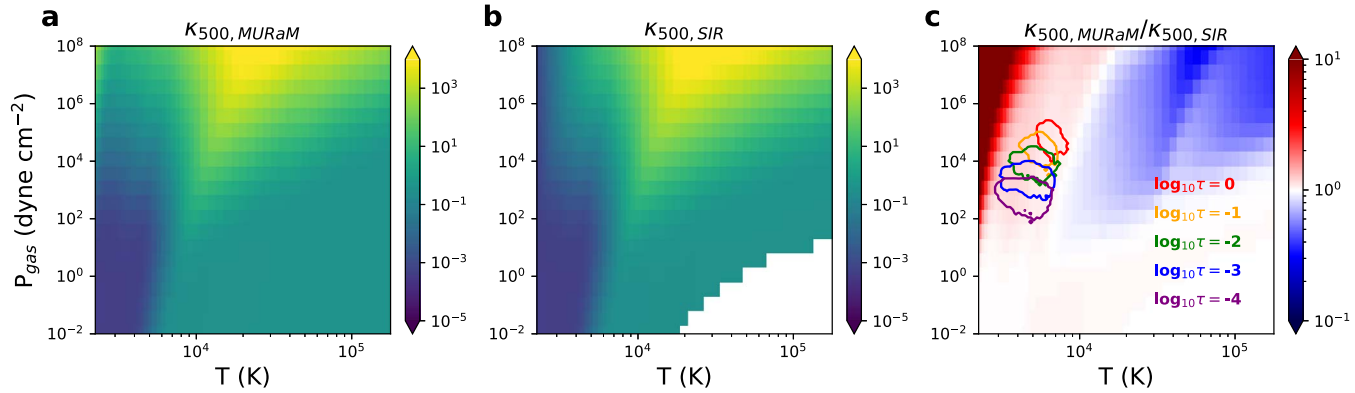

Figure 11. Panels (a) and (b) display the continuum opacity tables derived from the MURaM and SIR models, respectively. Panel (c) illustrates the ratio of these opacity tables, highlighting the pressure and temperature ranges with colored lines for Case 1 at $t = 5.4$ hr across various $\log_{10}\tau$ layers.

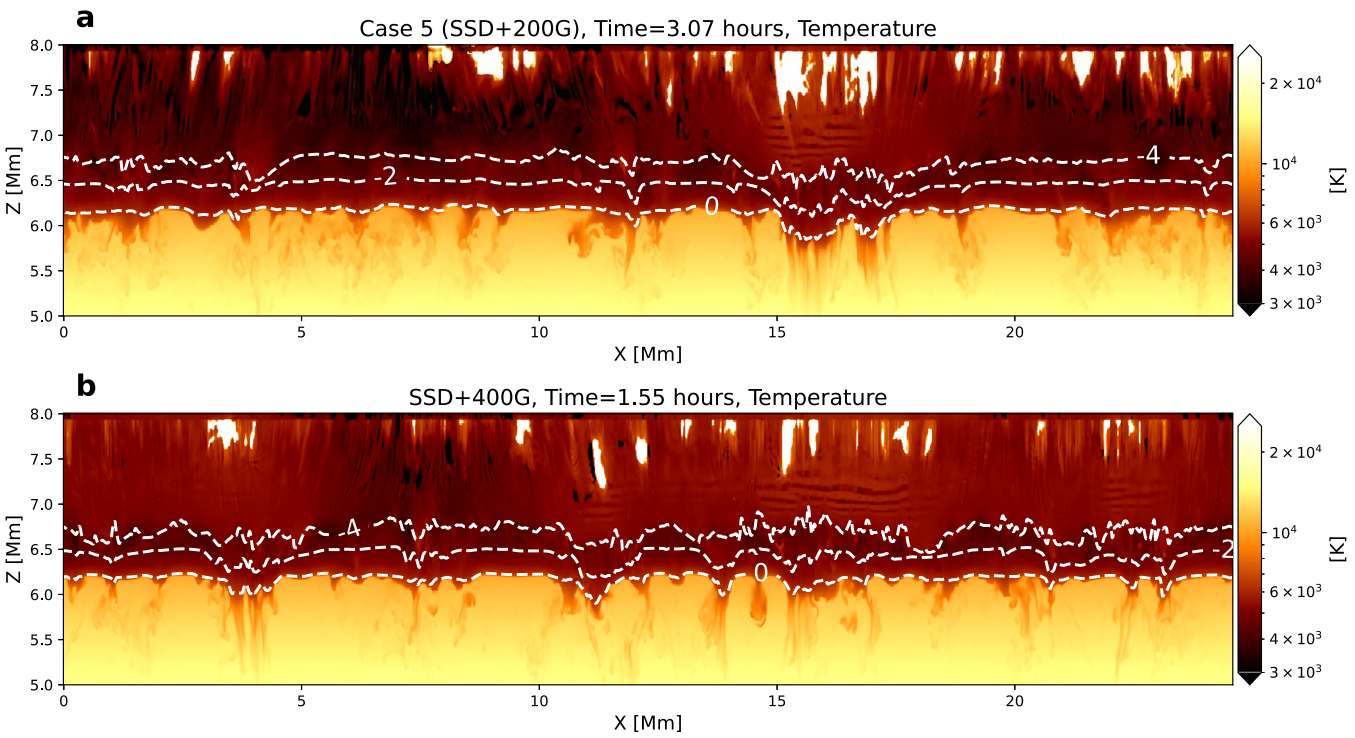

Figure 12. The oscillation in temperature in the vertical slice in the middle of the simulation box. Panels (a) and (b) show Case 5 and an additional test case with an added uniform field as large as 400 G. The three dotted curves are for $\log_{10}\tau = 0$, -2, and -4.

close to the top boundary. These are especially apparent for Case 5, with the strongest magnetic field of 200 G (Figure 12(a)). The root cause of this is that we artificially limited the Alfvén velocity v_A to 60 km s^{-1} to speed up the computation (M. Rempel et al. 2009; M. Rempel 2017). This is justified for our primary target, the photosphere, where v_A is low. However, numerical issues may arise in higher atmospheric layers, as v_A increases rapidly with decrease density such that the imposed limit becomes inconsistent with the calculation. To address this issue, we adjust the Courant–Friedrichs–Lewy (CFL) condition and Alfvén velocity limit as necessary to maintain numerical stability. The approach proves to significantly reduce the oscillation, though some residual signals remain. Other solutions include adding proper treatment for a transition region in higher layers. Unfortunately, this would lead to more than a tenfold increase in the required computing time, so was not adopted here.

It is worth noting that such oscillations do not appear in M. Rempel (2014), and they are barely detectable for the cases with a weaker mean magnetic field. Specifically, Case 5 is intermittently impacted, whereas Case 4 remains mostly unaffected. As a test, we also simulate a case with a stronger added magnetic field, 400 G, which produced even stronger oscillations (Figure 12(b)). The problem arises from both stronger magnetic fields and the more extended vertical domain. The combination leads to large v_A values exceeding the imposed limit. Efforts to stabilize this simulation by reducing the CFL parameter and adjusting the velocity parameters were unsuccessful. A potential solution involves expanding the simulation box upward and incorporating a realistic corona. This would significantly increase computational demands, exceeding the SPIn4D project's scope. Consequently, we limited our simulations to a maximum magnetic field strength of 200 G.

In both the 200 G and 400 G cases, we observed numerous "hot pockets" in the regions close to the top boundaries. In these regions, the code attempts to form a hot layer analogous to the transition region, but the set boundary conditions do not allow it to

do so. These hot pockets tend to extend to the lower region as the mean magnetic field increases. Meanwhile, temperatures outside these pockets above $z > 7$ Mm rise slightly with a stronger mean magnetic field, though the pockets themselves show little correlation with changes in the magnetic field.

We note that these aforementioned artifacts are not expected to impact our results, as illustrated by Figure 12. The upper panel (a) is for Case 5. The regions of numerical instability produce very high temperatures, exceeding 2×10^4 K, saturating the color table in white. These regions produce both the strong oscillations and shocks in the surrounding plasma, but are basically confined to strong-magnetic-field regions. The MURaM code uses a numerical diffusivity scheme that can significantly enhance the diffusivities in regions where the monotonicity changes (see Section 2 in M. Rempel 2014), where needed, and keep them low everywhere else. This sufficiently decays and prevents the spread of these oscillations to the lower and higher atmosphere, so they are mainly trapped around $z = 7$ Mm, where they are generated. The magnitude of the oscillations decreases as the density rises in the lower regions of the atmosphere, such that the oscillations are largely confined to layers where $\log_{10}\tau < -4$. Given the distribution of the response function, as shown in Figures 4(a)–(d), the regions critical for the formation of Fe I lines remain unaffected.

5. Summary

In this work, we provide an overview of the SPIn4D project, which aims at advancing the inversion of spectropolarimetric data through ML. We describe the procedures for generating a comprehensive training and test data set derived from MURaM simulations and the forward synthesis of Stokes profiles. Specifically, we conduct six distinct MURaM SSD simulations, generating a total of 109 TB of photospheric atmosphere data. Additionally, we synthesize Fe I lines at 630 and 1565 nm at every 12 minutes of the simulations, yielding 21 TB of data in HDF5 format. The simulations required an extensive computational effort, amounting to 10 million CPU hours. We have released the SIR-based synthesized Fe I lines and the corresponding 3D photospheric slabs totaling 13.7 TB, making them accessible to the wider research community for further analysis and study. We have used both the SIR and DeSIRe codes to synthesize the Stokes profiles. Their results largely agree; additional study is required to explain their minor differences. We will focus on the SIR results and keep the DeSIRe version available for the community. Our DL model training will use these MURaM simulations. The results and comparisons with the SIR inversion as a baseline will be presented in upcoming work.

This data set, encompassing photospheric physical variables from both quiet-Sun and Plage regions, is poised to bolster the burgeoning field of ML within solar physics. Its relevance extends particularly to the early research topics of the DKIST science objectives (M. P. Rast et al. 2021). The versatility of the data not only supports the inversion tasks of the SPIn4D project, but also potentially facilitates the development of a range of other ML models. The public availability of this data set ensures that the broader scientific community can leverage it not just for inversion studies, but also for other tasks, like advanced super-resolution and disambiguation of the horizontal magnetic field. The large volume can reduce the issue of overfitting when training DL models on a small data set. Its applicability is not limited to DKIST alone; other solar telescopes can also benefit from the insights derived from this comprehensive data set and the ML model built on it. In this way, the data set can act as a critical resource, driving forward the integration of ML techniques into solar physics and potentially transforming observational strategies and data analysis methodologies across multiple platforms.

Acknowledgments

We thank Carlos Quintero Noda for helpful discussions. This work is supported by NSF/AAG award #2008344, NSF/CAREER award #1848250 to the University of Hawai'i (UH), and the state of Hawai'i. J.L. acknowledges the support of the DKIST Ambassador program. This material is based upon work supported by the NSF National Center for Atmospheric Research, which is a major facility sponsored by the U.S. National Science Foundation under Cooperative Agreement No. 1852977. We would like to acknowledge high-performance computing support from Cheyenne (doi:10.5065/D6RX99HX) provided by NSF NCAR's Computational and Information Systems Laboratory (CISL), sponsored by the NSF. The technical support and advanced computing resources from UH Information Technology Services—Cyberinfrastructure, funded in part by the NSF CC* awards #2201428 and #2232862, are gratefully acknowledged. L.A.T, S.A.J., and T.A.S are supported by the National Solar Observatory.

Software: MURaM (A. Vögler et al. 2005; M. Rempel et al. 2009), SIR3D (B. Ruiz Cobo & J. C. del Toro Iniesta 1992, 2012), DeSIRe (B. Ruiz Cobo et al. 2022), Parallel Python wrapper (R. Gafeira et al. 2021), Matplotlib (J. D. Hunter 2007), and SciPy (P. Virtanen et al. 2020).

Appendix A
Changes in SIR3D and Data Organizing

To enhance the handling of half-integer quantum levels for the Fe I 1565 nm lines, new atomic state symbols have been updated in the `src/interface.f90` module of the 3D version of SIR. The orbital angular momentum range has been expanded from six integer levels to include 13 integer and 11 half-integer levels. The element abundance data were updated in both `src/interface.f90` and `src/leyendo.f`. We have enhanced the selection of optical depth ranges for forward synthesis by introducing new parameters in `synth/model.py`: `clip_tau`, `clip_tau_min`, and `clip_tau_max`. To address precision issues in the upper layers of MURaM simulations that cause duplication at very small optical depths, line synthesis is now constrained to layers within $-5 < \log_{10}\tau < 2$. We modified the SIR3D code to support a new "MURAM" atmosphere that uses solar Cartesian coordinates, to match the DL-NIRSP axis ordering and the conventions used in the Python package for the solar community (SunPy). MURaM's SSD simulation coordinates (z^m, y^m, x^m) correspond to SIR3D's coordinates (z^s, x^s, y^s) and to solar Cartesian coordinates (y^c, x^c, z^c), thus a `transpose(1,0,2)` transformation is applied to all `memmap` objects in `synth/multiprocessing.py` to align with the solar Cartesian coordinate system. See our project website for a detailed explanation of these changes.

On the SPIn4D project website, our data sets are stored within corresponding case directories, whose names are characterized by the mean magnetic field strength. The directories are labeled as follows: `SPIN4D_SSD`, `SPIN4D_SSD_50G`, `SPIN4D_SSD_50G_V`, `SPIN4D_SSD_100G`, `SPIN4D_SSD_200G`, and `SPIN4D_SSD_Large`, corresponding to Cases 1 through 6. For instance, the file `subdomain_0.051405` in the directory

SPIN4D_SSD_50G corresponds to the mass density data from the simulation output at time index "051405," where "0" is the variable index. Variable indices from 0 to 11 represent the mass density (ρ), velocities (v_z, v_x, v_y), internal energy (e), magnetic fields (B_z, B_x, B_y), temperature (T), pressure (P), electron number density (N_e), and optical depth (τ), the shift of the vector components reflecting the coordinate transformations between SIR and MURaM previously mentioned. Furthermore, stokes-051405-6302.h5 corresponds to the Fe I 630 nm line at the corresponding output time index. Detailed guidance on accessing and interpreting the data is provided in our online tutorial.[10] It is also available on Zenodo doi:10.5281/zenodo.13879854.

Appendix B
Comparison of Synthesized Lines

Statistical comparisons of the synthesized Stokes profiles for the 1565 nm line from SIR and DeSIRe are detailed in Figure 13. These discrepancies of the Stokes I and V are more obvious than those observed in the 630 nm lines shown in Figure 10. Specifically, for the 1565.2 nm line, DeSIRe exhibits greater slopes for Stokes Q and U compared to the identity relation. Despite these differences, the Pearson correlation coefficient remains above 0.939 for all line positions and all Stokes components, though it shows a weaker correlation than the 630 nm lines, whose smallest correlation is 0.969.

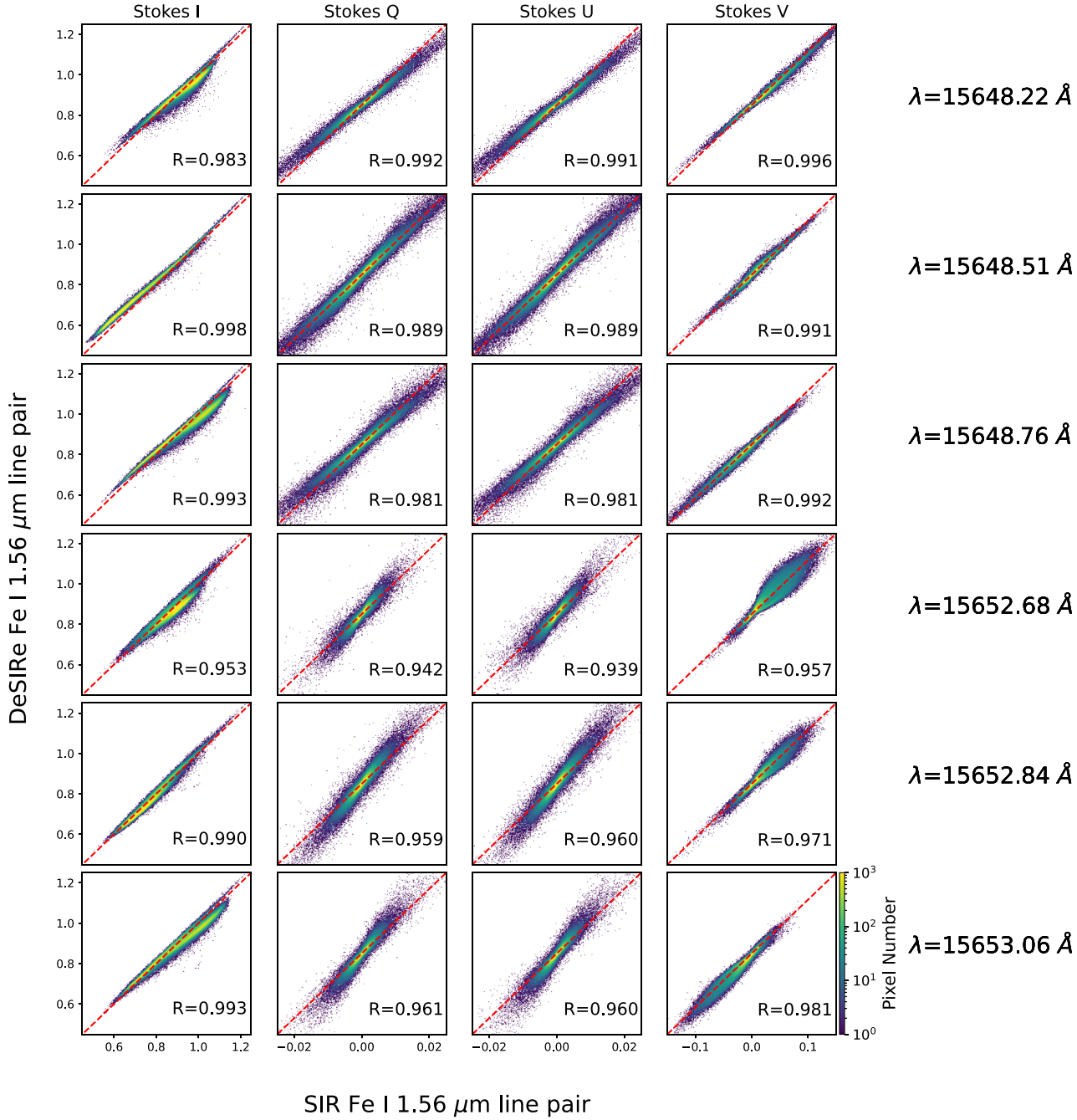

Figure 13. The same as Figure 10, but for the 1565 nm lines.

[10] https://github.com/ifauh/spin4d-data

ORCID iDs

Kai E. Yang (杨凯) https://orcid.org/0000-0002-7663-7652
Lucas A. Tarr https://orcid.org/0000-0002-8259-8303
Matthias Rempel https://orcid.org/0000-0001-5850-3119
S. Curt Dodds https://orcid.org/0000-0001-6311-146X
Sarah A. Jaeggli https://orcid.org/0000-0001-5459-2628
Peter Sadowski https://orcid.org/0000-0002-7354-5461
Thomas A. Schad https://orcid.org/0000-0002-7451-9804
Ian Cunnyngham https://orcid.org/0000-0001-5171-9144
Jiayi Liu (刘嘉奕) https://orcid.org/0000-0002-7290-0863
Yannik Glaser https://orcid.org/0000-0001-7217-9749
Xudong Sun (孙旭东) https://orcid.org/0000-0003-4043-616X

References

Antiochos, S. K. 1998, ApJL, 502, L181
Antiochos, S. K., DeVore, C. R., & Klimchuk, J. A. 1999, ApJ, 510, 485
Asensio Ramos, A., Cheung, M. C. M., Chifu, I., & Gafeira, R. 2023, LRSP, 20, 4
Asensio Ramos, A., de la Cruz Rodríguez, J., & Pastor Yabar, A. 2018, A&A, 620, A73
Asensio Ramos, A., & Diaz Baso, C. J. 2019, A&A, 626, A102
Asensio Ramos, A., Requerey, I. S., & Vitas, N. 2017, A&A, 604, A11
Asensio Ramos, A., Trujillo Bueno, J., & Landi Degl'Innocenti, E. 2008, ApJ, 683, 542
Asplund, M., Grevesse, N., Sauval, A. J., & Scott, P. 2009, ARA&A, 47, 481
Barklem, P. S., Anstee, S. D., & O'Mara, B. J. 1998, PASA, 15, 336
Bellot Rubio, L., & Orozco Suárez, D. 2019, LRSP, 16, 1
Bobra, M. G., & Couvidat, S. 2015, ApJ, 798, 135
Bobra, M. G., & Ilonidis, S. 2016, ApJ, 821, 127
Borrero, J. M., & Pastor Yabar, A. 2023, A&A, 669, A122
Borrero, J. M., Pastor Yabar, A., Rempel, M., & Ruiz Cobo, B. 2019, A&A, 632, A111
Borrero, J. M., Pastor Yabar, A., & Ruiz Cobo, B. 2021, A&A, 647, A190
Brehmer, J., Louppe, G., Pavez, J., & Cranmer, K. 2020, PNAS, 117, 5242
Campbell, R. J., Keys, P. H., Mathioudakis, M., et al. 2023, ApJL, 955, L36
Castelli, F., & Kurucz, R. L. 2004, A&A, 419, 725
Centeno, R., Flyer, N., Mukherjee, L., et al. 2022, ApJ, 925, 176
Chappell, B. A., & Pereira, T. M. D. 2022, A&A, 658, A182
Chen, F., Cheung, M. C. M., Rempel, M., & Chintzoglou, G. 2023a, ApJ, 949, 118
Chen, F., Rempel, M., & Fan, Y. 2017, ApJ, 846, 149
Chen, F., Rempel, M., & Fan, Y. 2023b, ApJL, 950, L3
Cheung, M. C. M., Rempel, M., Chintzoglou, G., et al. 2019, NatAs, 3, 160
Cheung, M. C. M., Rempel, M., Title, A. M., & Schüssler, M. 2010, ApJ, 720, 233
Chitta, L. P., Peter, H., Young, P. R., & Huang, Y. M. 2017, A&A, 605, A49
de la Cruz Rodriguez, J., Leenaarts, J., Danilovic, S., & Uitenbroek, H. 2019, A&A, 623, A74
da Silva Santos, J. M., Reardon, K., Cauzzi, G., et al. 2023, ApJL, 954, L35
de Wijn, A. G., Casini, R., Carlile, A., et al. 2022, SoPh, 297, 22
del Toro Iniesta, J. C. 2007, Introduction to Spectropolarimetry (Cambridge: Cambridge Univ. Press)
del Toro Iniesta, J. C., & Ruiz Cobo, B. 2016, LRSP, 13, 13
Díaz Baso, C. J., & Asensio Ramos, A. 2018, A&A, 614, A5
Díaz Baso, C. J., Asensio Ramos, A., & de la Cruz Rodríguez, J. 2022, A&A, 659, A165
Díaz Baso, C. J., de la Cruz Rodríguez, J., & Danilovic, S. 2019, A&A, 629, A99
Eklund, H. 2023, A&A, 669, A106
Florios, K., Kontogiannis, I., Park, S.-H., et al. 2018, SoPh, 293, 28
Gafeira, R., Orozco Suárez, D., Milić, I., et al. 2021, A&A, 651, A31
Goodwin, G. T., Sadykov, V. M., & Martens, P. C. 2024, ApJ, 964, 163
Grevesse, N., & Sauval, A. J. 1998, SSRv, 85, 161
Harrington, D. M., Sueoka, S. R., Schad, T. A., et al. 2023, SoPh, 298, 10
Higgins, R. E. L., Fouhey, D. F., Antiochos, S. K., et al. 2022, ApJS, 259, 24
Higgins, R. E. L., Fouhey, D. F., Zhang, D., et al. 2021, ApJ, 911, 130
Huang, X., Wang, H., Xu, L., et al. 2018, ApJ, 856, 7
Hubeny, I., & Mihalas, D. 2015, Theory of Stellar Atmospheres. An Introduction to Astrophysical Non-equilibrium Quantitative Spectroscopic Analysis (Princeton, NJ: Princeton Univ. Press)
Hunter, J. D. 2007, CSE, 9, 9
Jaeggli, S. A., Lin, H., Onaka, P., et al. 2022, SoPh, 297, 137
Jarolim, R., Thalmann, J. K., Veronig, A. M., & Podladchikova, T. 2023, NatAs, 7, 1171
Jarolim, R., Tremblay, B., Muñoz-Jaramillo, A., et al. 2024a, ApJL, 961, L31
Jarolim, R., Tremblay, B., Rempel, M., et al. 2024b, ApJL, 963, L21
Kazachenko, M. D., Fisher, G. H., & Welsch, B. T. 2014, ApJ, 795, 17
Kuridze, D., Uitenbroek, H., Wöger, F., et al. 2024, ApJ, 965, 15
Lites, B. W., Kubo, M., Socas-Navarro, H., et al. 2008, ApJ, 672, 1237
Liu, C., Xu, Y., Cao, W., et al. 2016, NatCo, 7, 13104
Liu, Y., Hoeksema, J. T., Bobra, M., et al. 2014, ApJ, 785, 13
Liu, Y., & Schuck, P. W. 2012, ApJ, 761, 105
Liu, Y., Welsch, B. T., Valori, G., et al. 2023, ApJ, 942, 27
Lord, J. W. 2014, PhD thesis, Univ. of Colorado, Boulder
Lord, J. W., Cameron, R. H., Rast, M. P., Rempel, M., & Roudier, T. 2014, ApJ, 793, 24
Lumme, E., Kazachenko, M. D., Fisher, G. H., et al. 2019, SoPh, 294, 84
Milić, I., & Gafeira, R. 2020, A&A, 644, A129
Milić, I., & van Noort, M. 2018, A&A, 617, A24
Mistryukova, L., Plotnikov, A., Khizhik, A., et al. 2023, SoPh, 298, 98
Moore, R. L., Sterling, A. C., Hudson, H. S., & Lemen, J. R. 2001, ApJ, 552, 833
Nishizuka, N., Sugiura, K., Kubo, Y., Den, M., & Ishii, M. 2018, ApJ, 858, 113
Pastor Yabar, A., Borrero, J. M., & Ruiz Cobo, B. 2019, A&A, 629, A24
Priest, E. 2014, Magnetohydrodynamics of the Sun (Cambridge: Cambridge Univ. Press)
Priest, E. R., & Forbes, T. G. 2002, A&ARv, 10, 313
Quintero Noda, C., Barklem, P. S., Gafeira, R., et al. 2021, A&A, 652, A161
Quintero Noda, C., Khomenko, E., Collados, M., et al. 2023, A&A, 675, A93
Rahman, S., Jeong, H.-J., Siddique, A., Moon, Y.-J., & Lawrance, B. 2024, ApJS, 271, 14
Rahman, S., Moon, Y.-J., Park, E., et al. 2020, ApJL, 897, L32
Rahman, S., Shin, S., Jeong, H.-J., et al. 2023, ApJ, 948, 21
Rast, M. P., Bello González, N., Bellot Rubio, L., et al. 2021, SoPh, 296, 70
Rempel, M. 2012, ApJ, 750, 62
Rempel, M. 2014, ApJ, 789, 132
Rempel, M. 2017, ApJ, 834, 10
Rempel, M., Schüssler, M., & Knölker, M. 2009, ApJ, 691, 640
Rimmele, T. R., Warner, M., Keil, S. L., et al. 2020, SoPh, 295, 172
Ruiz Cobo, B., & del Toro Iniesta, J. C. 1992, ApJ, 398, 375
Ruiz Cobo, B., & del Toro Iniesta, J. C., 2012 SIR: Stokes Inversion Based on Response functions, Astrophysics Source Code Library, ascl:1212.008
Ruiz Cobo, B., Quintero Noda, C., Gafeira, R., et al. 2022, A&A, 660, A37
Sadowski, P., & Baldi, P. 2018, in Deep Learning in the Natural Sciences: Applications to Physics, ed. L. Rozonoer, B. Mirkin, & I. Muchnik (Cham: Springer), 269
Sainz Dalda, A., de la Cruz Rodríguez, J., De Pontieu, B., & Gošić, M. 2019, ApJL, 875, L18
Samanta, T., Tian, H., Yurchyshyn, V., et al. 2019, Sci, 366, 890
Schad, T. A., Kuhn, J. R., Fehlmann, A., et al. 2023, ApJ, 943, 59
Schmidt, W., Schubert, M., Ellwarth, M., et al. 2016, Proc. SPIE, 9908, 99084N
Schuck, P. W., & Antiochos, S. K. 2019, ApJ, 882, 151
Smitha, H. N., Holzreuter, R., van Noort, M., & Solanki, S. K. 2020, A&A, 633, A157
Smitha, H. N., Holzreuter, R., van Noort, M., & Solanki, S. K. 2021, A&A, 647, A46
Socas-Navarro, H., de la Cruz Rodríguez, J., Asensio Ramos, A., Trujillo Bueno, J., & Ruiz Cobo, B. 2015, A&A, 577, A7
Song, W., Ma, W., Ma, Y., Zhao, X., & Lin, G. 2022, ApJS, 263, 25
Stenflo, J. 1994, Solar Magnetic Fields: Polarized Radiation Diagnostics, 189 (Berlin: Springer)
Stenflo, J. O. 2012, A&A, 547, A93
Sun, X., Hoeksema, J. T., Liu, Y., et al. 2013, ApJ, 778, 139
Thalmann, J. K., Georgoulis, M. K., Liu, Y., et al. 2021, ApJ, 922, 41
Tremblay, B., Roudier, T., Rieutord, M., & Vincent, A. 2018, SoPh, 293, 57
Uitenbroek, H. 2001, ApJ, 557, 389
Vicente Arévalo, A., Asensio Ramos, A., & Esteban Pozuelo, S. 2022, ApJ, 928, 101
Virtanen, P., Gommers, R., Oliphant, T. E., et al. 2020, NatMe, 17, 261
Vögler, A. 2004, A&A, 421, 755
Vögler, A., & Schüssler, M. 2007, A&A, 465, L43
Vögler, A., Shelyag, S., Schüssler, M., et al. 2005, A&A, 429, 335
Wang, H., Cao, W., Liu, C., et al. 2015, NatCo, 6, 7008
Wang, H., Liu, C., Ahn, K., et al. 2017, NatAs, 1, 0085
Wang, Z., Bovik, A. C., Sheikh, H. R., & Simoncelli, E. P. 2004, ITIP, 13, 600
Welsch, B. T. 2015, PASJ, 67, 18
Wyper, P. F., Antiochos, S. K., & DeVore, C. R. 2017, Natur, 544, 452